

## DECI Project Report

# A New Modelling Approach for Turbulent Astrophysical Flows

Wolfram Schmidt, Jens C. Niemeyer,  
Markus Hupp, Christoph Federrath and Andreas Maier

March 19, 2007

## 1 Introduction

Almost all problems of astrophysical hydrodynamics share two important attributes: first, the ubiquitous presence of spatially localised features such as shocks, clumps, or composition discontinuities that need to be numerically resolved or at least adequately modelled; and second, large Reynolds numbers ( $Re > 10^{14}$ ) indicating that fully developed, i.e. space-filling, turbulence is responsible for the mixing and dissipation properties of the gas almost everywhere. Despite great advances in computational fluid dynamics, an accurate handling of both aspects has so far proven to be very difficult as specialised numerical techniques have seemed to be mutually incompatible.

Considerable progress has been made in modelling as much flow structure as possible by direct numerical computation. The most powerful method for the treatment of non-steady flows exhibiting significant anisotropy and high degrees of intermittency is adaptive mesh refinement (AMR). AMR is based on Eulerian continuum mechanics with a hierarchy of grid patches to approximate the flow on various levels of resolution [Berger and Olinger \[1984\]](#). In localised regions developing structure on comparatively small length scales, a higher level of refinement is applied while smoother portions of the flow are treated with coarser grids. Astrophysical problems for which AMR is particularly well suited include strong shocks [Berger and Colella \[1989\]](#) and gravitational collapse [O'Shea et al. \[2004\]](#) among many other applications [Norman \[2004\]](#). All cases exhibit locally steep gradients of the state variables and/or rapid spatiotemporal changes in the velocity field.

Until very recently, AMR has been considered inappropriate for the treatment of fully developed, space filling turbulence. The traditional argument against AMR is that high levels of refinement would be required virtually everywhere. However, the picture of isotropic turbulence holds only with respect to an ensemble average.

In fact, dissipation is concentrated in spatial regions of dimension less than three at a any instant of time. In the case of subsonic turbulence, dissipation occurs mostly in vortex filaments, whereas sheets are the locus of dissipation in supersonic turbulence. This fact motivated the novel application of AMR to the simulation of forced turbulence by Kritsuk and Norman [Kritsuk et al. \[2006\]](#).

In the project reported below, we systematically investigated under which conditions simulations of compressible, forced turbulence can benefit from the application of AMR. In order to retain as much generality as possible, rather than trying to model a specific astrophysical environment we divided the most important occurrences of supersonic turbulence in astrophysics into two universality classes, described respectively by an adiabatic or an isothermal equation of state. The former serves as a model for the hot, fully ionised gas in galaxy clusters or near supernova remnants, while the latter is representative for the cold medium in giant molecular clouds with effective radiative cooling. In both cases, comparative simulations were performed with a static grid and with AMR, where several novel refinement criteria derived from properties of the velocity gradient were employed for the latter. Results are presented in terms of the density and vorticity distribution functions, the energy power spectrum, and the velocity structure functions.

## 2 Numerical Techniques

We employed the open source AMR code [Enzo](#). This code was specifically designed for astrophysical applications, in particular, the simulation of self-gravitating compressible gas dynamics [\[O’Shea et al., 2004\]](#). The fluid dynamical core of Enzo is based on the piece-wise parabolic method [\[Colella and Woodward, 1984\]](#). Enzo supports multi-level adaptive mesh refinement, parallel runs with MPI and output in the versatile HDF5 format.

For our project, we implemented several additions to the code. Kinetic energy is supplied to the flow by means of an Ornstein-Uhlenbeck-type driving force that comprises predominantly compressive modes [\[Schmidt et al., 2006\]](#). The discrete Fourier modes of the acceleration  $\hat{\mathbf{a}}_{jlm}(t)$  are determined by the following Langevin-type stochastic differential equation:

$$d\hat{\mathbf{a}}_{jlm}(t) = g_\zeta \left[ -\hat{\mathbf{a}}_{jlm}(t) \frac{dt}{T} + \frac{V}{T} \left( \frac{2\sigma^2(\mathbf{k})}{T} \right)^{1/2} \mathbf{P}_\zeta(\mathbf{k}_{jlm}) \cdot d\mathbf{W}_t \right]. \quad (1)$$

The second term generates Gaussian random deviates ( $\mathbf{W}_t$  is called the *Wiener process*). There are non-zero modes for  $|\mathbf{k}| \in [0, 2k_0]$ , where  $k_0 = 2\pi\alpha/X$  is the characteristic wavenumber for a cubic domain of size  $X$ . In the simulations presented here,  $\alpha = 2$  (i. e., the forcing wavelength is about half of the domain size). The autocorrelation time scale  $T$  is identified with the large-eddy turn-over time, i. e.,  $T = L/V$ , where  $V$  is the characteristic velocity of the flow in the stationary regime and  $L = X/\alpha = 2\pi/k_0$  is the integral length.

For purely solenoidal forcing, the random deviates are projected perpendicular to the associated wave vectors  $\mathbf{k}_{jlm}$  by means of the projection operator

$$(P_{ij})_{\zeta}(\mathbf{k}) = \zeta P_{ij}^{\perp}(\mathbf{k}) + (1 - \zeta) P_{ij}^{\parallel}(\mathbf{k}) = \zeta \delta_{ij} + (1 - 2\zeta) \frac{k_i k_j}{k^2}. \quad (2)$$

with  $\zeta = 1$ . In the case  $\zeta = 0$ , on the other hand, projection parallel to the wave vectors results in a dilatational forcing field compressing or rarifying rather than stirring the gas. We set  $\zeta = 0.1$ . Thus, compression dominates over rotation in our simulations. This feature was motivated by the presumably mostly compressive driving in the interstellar medium. Due to the normalisation factor

$$g_{\zeta} = \frac{1}{1 - 2\zeta + 3\zeta^2} \quad (3)$$

in equation (1), the root mean square acceleration  $a_{\text{rms}} = \sqrt{3}V/T$  is independent of  $\zeta$ . We chose  $V = 5c_0/\sqrt{3}$ , where  $c_0$  is the initial speed of sound. The corresponding expectation value of the velocity in the statistically stationary regime is  $5c_0$  implying a Mach 5 turbulent flow provided that the gas is isothermal. If the dissipated kinetic energy is added to the internal energy, on the other hand, the heating of the gas implies an increasing speed of sound and, thus, a gradually declining Mach number. For this reason, the characteristic Mach number corresponds to the peak Mach number in adiabatic turbulent gas.

In the first phase of the project, we used static grids to run direct numerical simulations of forced isotropic turbulence starting with homogeneous gas at rest (see the next Section). In the following phase, adaptive mesh refinement was applied (Section 4). To that end, various refinement criteria based on so-called structural quantities were investigated. Structural quantities are velocity derivatives such as the rate of strain and vorticity. For the computation of these quantities and the implementation of the new refinement criteria, further components were added to Enzo.

### 3 Static grid simulations

In the following, we present and discuss a couple of highly resolved simulations of forced isotropic turbulence on static grids with  $N = 768^3$  cells. These simulations were slightly less ambitious than the originally proposed  $N = 10^9$  simulations due to the restriction of MPI-programs to single 126-CPU partitions of SARA-ASTRA.

As mentioned in the previous Section, the characteristic Mach numbers was set to  $\text{Ma} = V/c_0 = 5.0$  in both simulations. The actual RMS Mach numbers found in the course of the simulations, however, turned out to be somewhat less because of mostly dilatational forcing and, in addition, the gradual heating of the gas in the adiabatic case. The data obtained from the simulations were analysed in terms of probability density functions, energy spectrum functions and structure functions. We will discuss the results both for the adiabatic and the isothermal case.

### 3.1 Adiabatic turbulence

If the heat generated by kinetic energy dissipation remains within the system, the flow will evolve adiabatically. In Enzo, the dissipation of kinetic energy is solely of numerical origin. This means that PPM smoothes the flow at the smallest resolved length scales and the loss of kinetic energy is balanced by an increase in the internal energy. Since the forcing field continually injects mechanical energy into the system, it is implied that the total energy rises as well. For the adiabatic exponent  $\gamma$  in the relation between pressure and density,  $P \propto \rho^\gamma$ , we set  $\gamma = 1.4$ .

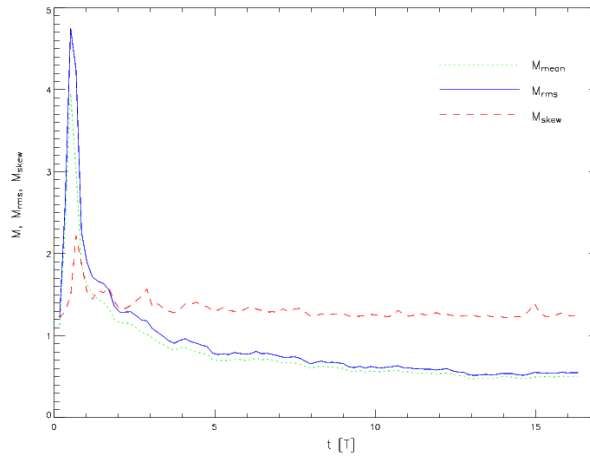


Figure 1: Temporal evolution of the mean, the root mean square and the skewness (first, second and third moment) of the local Mach number  $v/c_s$  in the adiabatic case.

As a consequence of the ever increasing heat content of the gas in the course of the simulation, the speed of sound grows relative to the root mean square velocity of the flow, once turbulence is fully developed. As a consequence, the turbulent flow will evolve toward the limit of incompressibility, in which the internal energy and, hence, the speed of sound ceases to affect the fluid dynamics. In order to investigate the asymptotic behaviour, it was necessary to run the simulation over more than 15 integral time scales which consumed a great deal of computational resources. The first three statistical moments of the local Mach number  $v/c_s$  as functions of time are plotted in Figure 1. After a pronounced maximum at  $t \approx 0.5T$ , the Mach number quickly drops down into the transonic regime.  $\text{Ma}_{\text{rms}} = 1$  is reached at  $t \approx 3.0T$  and thereafter slowly decreases further with a final value  $\text{Ma}_{\text{rms}} \approx 0.5$ . This result indicates that, in the subsonic regime, the turbulent flow reaches a state, in which secular changes become apparent over a significantly greater interval of time than the dynamical time scale  $T$ .

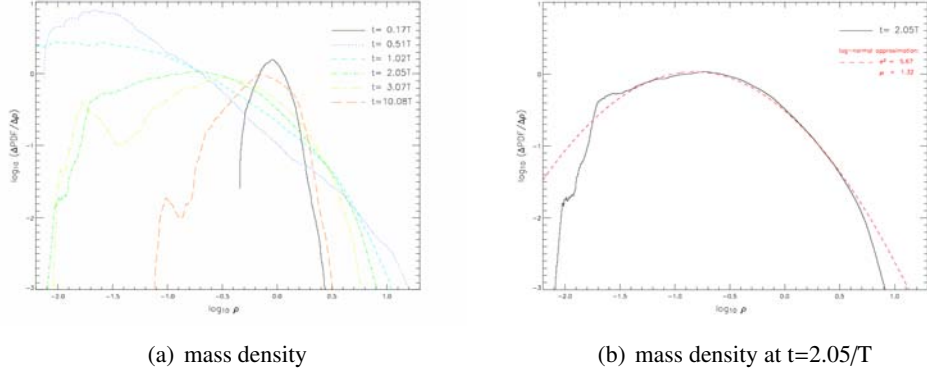


Figure 2: Temporal evolution of the density probability distribution function ( $\rho$ -pdf) of the adiabatic simulation run at six instances in time (a) and with lognormal fit at time  $t = 2.0T$  (b).

### 3.1.1 Mass density

Probability density functions (pdfs) show the variability of dynamical quantities in a flow realization at a certain instant of time. The integrated probability densities are called the probability distribution functions (PDF). The pdfs of mass density at several representative stages in the flow evolution are plotted in Figure 2. Note that scale is double-logarithmic. We see, that in the beginning the density  $\rho$ -pdf (black, solid line) is centred neatly around the initial density value  $\rho_0 = 1$ . During the early evolution, the density distribution gradually shifts towards low densities and simultaneously develops a long tale in the high density regime. After approximately one and a half integral time ( $t \approx 1.5T$ ), this trend is reversed and the density maximum is displaced back towards lower densities. This reflects the deteriorating compressibility of the gas following the onset of turbulence energy dissipation. At late time ( $t \gtrsim 10T$ ), the  $\rho$ -pdf settles into a comparatively slowly changing distribution with its maximum close to the initial value.

Following Padoan and Nordlund [2002] we applied fits of a lognormal distribution (eq. 4) to the  $\rho$ -pdfs and concluded that the overall behaviour of the simulated gas densities are well described by

$$dp(\rho) = \frac{1}{\sqrt{2\pi}\sigma\rho} \exp\left[-\frac{(\ln\rho - \mu)^2}{2\sigma^2}\right]d\rho. \quad (4)$$

An example for a  $\rho$ -pdf and the corresponding fit function is plotted in Figure 2 (b). However, it is also obvious from the simulation, that the high density tail of the analysed distributions are overestimated by the lognormal approximation. For our eventual goal to derive a model describing the gas distribution in star formation (SF) regions, adopting lognormal-fitted  $\rho$ -pdfs would thus result in a systematic

overestimate of high density regions where SF is most efficient.

In the high Mach number regime, the  $\rho$ -pdfs display a pronounced skewness towards low density regions. This is a consequence of shocks compressing gas in thin sheetlike regions with relatively small volume filling factors. On the other hand, the depletion of gas in the surroundings of the shocks results in voids which are represented by the low-density tail of the pdfs. In the isothermal case it becomes apparent that the shocks tend to break up in smaller eddy-like entities with the  $\rho$ -pdfs, thus, more resembling log-normal distributions.

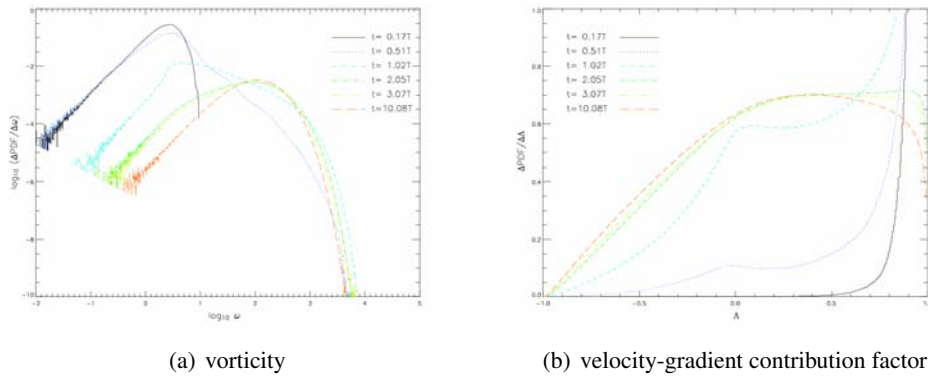


Figure 3: Temporal evolution of the pdfs of  $\omega$  and  $\Lambda$ , respectively.

### 3.1.2 Vorticity and Strain

The curl of the velocity field,  $\boldsymbol{\omega} = \nabla \times \boldsymbol{v}$ , is called vorticity. The pdfs of the vorticity modulus  $\omega = |\nabla \times \boldsymbol{v}|$  displayed in Figure 3 can be used to analyse the amount of circulation or more precisely the local angular rate of rotation within the simulated gas. Starting from the initial setup, the solenoidal component of the driving force stirs the gas into rotational motion on the largest scales. This results in eddies appearing as low amplitude vorticity at the left-hand side of the pdfs. As the turbulence cascade produces smaller and smaller eddies, the distribution broadens initially. Near the peak of the Mach number shown in Figure 1, the pdf assumes a shape that is typical for supersonic turbulence. In between the low and high vorticity tails, there is an intermediate range exhibiting approximate power-law behaviour. After the transition to subsonic flow, the simpler  $\omega$ -pdf found for nearly incompressible turbulence emerges.

The importance of strain caused by steep velocity gradients relative to eddy-like structures becomes apparent in the pdfs of the so-called velocity-gradient contribution factor  $\Lambda$  which is defined by

$$\Lambda = \frac{|S|^2 - \omega^2}{|S|^2 + \omega^2}. \quad (5)$$

The rate-of-strain scalar is obtained from the total contraction of the symmetric part of the velocity gradient, i. e.  $|S|^2 = 2S_{ij}S_{ij}$ , where  $S_{ij} = \frac{1}{2}(v_{i,j} + v_{j,i})$ . The  $\Lambda$ -pdfs show that initially the flow is dominated by  $\Lambda > 0$ . This is mostly caused by velocity gradients arising from non-rotational fluid motion and the production of shocks. Somewhat later, the growing vorticity of the flow gives rise to an increasing volume fraction with  $\Lambda < 0$ . Remarkably, the pdf appears to change very little once the value of  $\text{Ma}_{\text{rms}}$  drops below unity.

## 3.2 Isothermal turbulence

In the limiting case that all heat produced by the dissipation is removed by heat transfer from the system immediately, the gas evolves isothermally. In the interstellar medium, heat is transferred by radiation with high efficiency provided that the gas density is sufficiently low. Nearly isothermal turbulence can be simulated by setting  $\gamma = 1.01$ . Then  $P \simeq \rho c_s^2$ , where  $c_s$  is approximately equal to the constant isothermal speed of sound. For  $\text{Ma}^2 \sim 10$ , the specific kinetic energy  $e_{\text{kin}} \sim 10c_s^2$  and the internal energy density  $e_{\text{int}} = P/(\gamma - 1)\rho \sim 100c_s^2$ . Thus, the dissipation of kinetic energy results in a relative change of the internal energy that is smaller by one order of magnitude. In this sense, the gas is nearly isothermal.

### 3.2.1 Mass density

In the adiabatic case, compressive heating produces additional pressure and, hence, the gas increasingly resists further compression. In isothermal gas, on the other hand, the pressure increases proportional to the mass density which implies a scaling of density fluctuations with the Mach number squared. Therefore we expect the  $\rho$ -pdfs to show stronger fluctuations and, indeed, we find this behaviour as can be seen in Figure 4 (a). To reach a better statistical convergence, the pdfs were averaged over five samples separated by intervals of 0.725 integral time scales. Albeit the averaged pdfs still differ in the low density regime, which mainly reflects changes in the large scale structure of the flow, the distribution of mass density appears to be well converged for  $\rho/\langle\rho\rangle \gtrsim 0.1$  from  $t > 1.0T$  onwards. Therefore, isothermal turbulence approaches statistical equilibrium roughly within one integral time.

### 3.2.2 Vorticity

In the early phase of the simulation ( $t < 1.0T$ ), the pdfs of vorticity plotted in Figure 4b are qualitatively similar to those found in the adiabatic run. In particular, the  $\omega$ -pdf at  $t = 1.02T$  shows an intermediate power-law subrange comparable to the corresponding pdf in Figure 3. During the late evolution of the simulation, however, the distribution remains much broader than in the adiabatic case, because there is no transition from supersonic to subsonic turbulence. This can be interpreted as a consequence of a higher fraction of spatially extended low-vorticity

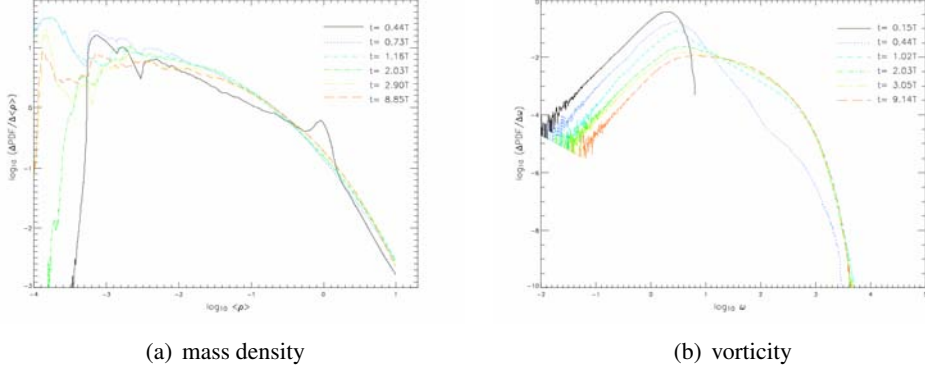


Figure 4: Temporal evolution of  $\rho$  and  $\omega$ -pdfs for nearly isothermal turbulence. The  $\rho$ -pdfs are averaged over several samples.

$t/T$	$\beta$
1.02	$1.97 \pm 0.02$
2.03	$1.78 \pm 0.03$
3.05	$1.75 \pm 0.03$
4.06	$1.78 \pm 0.03$
4.93	$1.78 \pm 0.03$
5.95	$1.77 \pm 0.03$

Table 1: Power-law exponents of the energy spectrum function  $E(k) \sim k^{-\beta}$  obtained from least-squares fits in the wavenumber range  $3 < kL/2\pi < 20$  at different instances in time. The error margins indicate standard deviations.

structures in supersonic turbulent flow in comparison to small-scale eddies of high vorticity which dominate in subsonic turbulence.

### 3.2.3 Energy spectrum functions

The sequence of energy spectrum functions for consecutive instants of time shown in Figures 5 and 6, illustrates the gradual build-up of the turbulent energy cascade in the course of the first integral time scale followed by the relaxation of the system into statistical equilibrium. The spectrum at  $t \approx 1.0T$  can be well fitted by a power-law  $E(k) \sim k^{-1.97 \pm 0.02}$  that is steeper than the Kolmogorov spectrum  $E(k) \sim k^{-5/3}$  and thus, indicates supersonic turbulence. In each plot, a line with slope  $-5/3$  allows for comparison with Kolmogorov scaling. Least-squares fits in the wavenumber range  $3 < kL/2\pi < 20$  show a minor flattening of the spectra with  $E(k) \sim k^{-1.77 \pm 0.04}$  after a few integral time scales have elapsed. The expo-

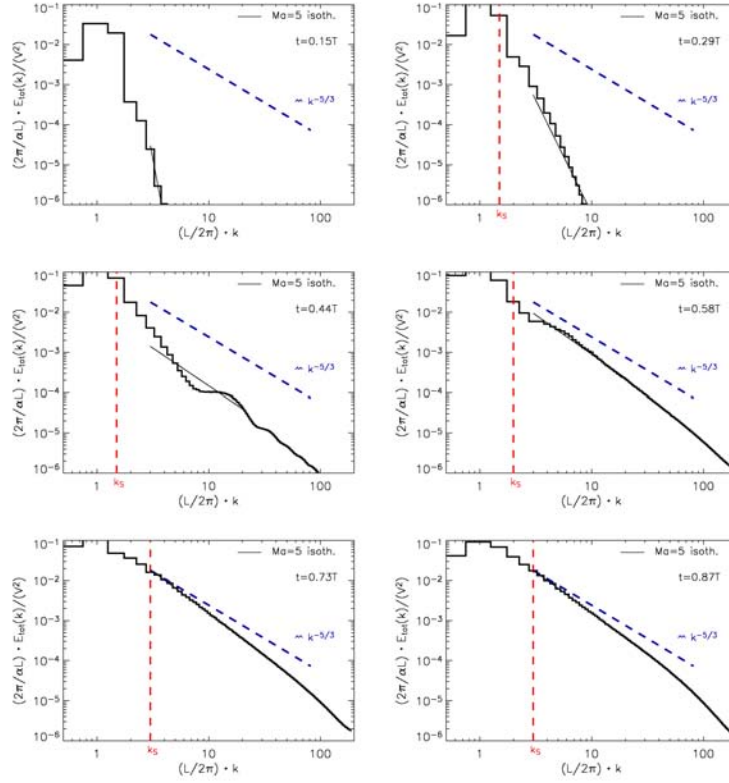


Figure 5: Early evolution of the energy spectra at several instants of time  $t < T$ . The sonic scale is indicated as vertical dotted line. Additionally the Kolmogorov slope  $-5/3$  is depicted as dashed line.

ments are summarised in Table 1. However, even the late-time spectra are steeper than  $E(k) \propto k^{-1.67}$  as predicted by Kolmogorov for incompressible turbulence. There is however good agreement with the theory of Boldyrev [2002], in which  $E(k) \sim k^{-1.74}$  is obtained for supersonic turbulence. Since the RMS Mach number permanently remains greater than unity for  $t > 1.0T$ , deviations from Kolmogorov theory are to be expected. The small bump in the spectrum functions that can be seen in the vicinity of  $kL/2\pi \approx 30$  at least partially stems from the so-called bottleneck effect (e. g. Schmidt et al. [2006]). For large wavenumbers, the damping of velocity fluctuations due to the numerical dissipation of PPM becomes noticeable.

An important parameter of supersonic turbulence is the sonic wavenumber  $k_s$  for which the turbulent velocity fluctuations are comparable to the speed of sound, i. e.  $v'(\ell_s) \sim c_s$ , where  $\ell_s = 2\pi/k_s$ . For smaller wavenumbers,  $k \lesssim k_s$ , the flow is highly compressible and the Fourier modes of the velocity field can be dilatational as well as solenoidal. Towards  $k \gg k_s$ , on the other hand, the flow becomes asymptotically incompressible. More specifically, we define the sonic wavenumber

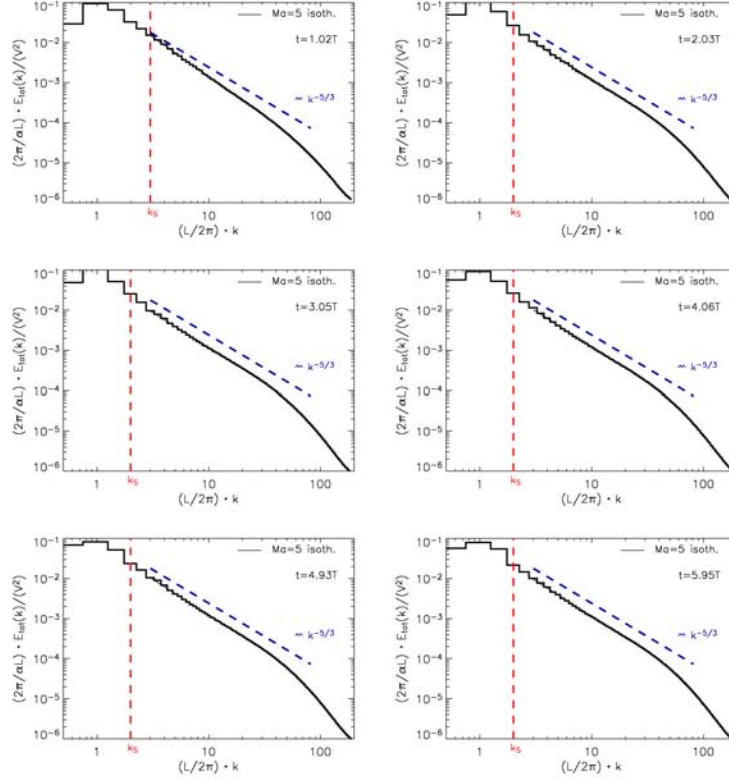


Figure 6: Temporal evolution of the energy spectra continuing Figure 5 for  $t > T$ .

$k_s$  implicitly by

$$\int_{k_s}^{\infty} E(k) dk = \frac{1}{2} \langle c_s^2 \rangle. \quad (6)$$

Thus, the cumulative turbulence energy in the range  $k \gtrsim k_s$  is identified with  $\frac{1}{2} \langle c_s^2 \rangle$ . Numerically, the integral can be evaluated only up to the cutoff wavenumber  $\pi/\Delta$ . The resulting sonic wavenumbers are indicated by vertical lines in Figures 5 and 6. Due to moderate RMS Mach number,  $k_s$  never becomes greater than  $3k_0$ , where  $k_0$  is the characteristic wavenumber of the driving force, throughout the simulation. It is interesting to note, however, that  $k_s$  reaches a maximum after about one integral time has elapsed and afterwards settles at a steady state value  $k_s \approx 2k_0$ . Together with the maximum of  $k_s$  comes the steepest energy spectrum function with an exponent of  $\approx -2.0$ . At later time,  $E(k)$  tends to be closer to the Kolmogorov spectrum. This behaviour is illustrated by the sequence of three-dimensional renderings of  $\omega$ -isosurfaces shown in Figures 7 and 8. In the course of the first integral time, turbulence is developing and extended sheetlike structures are emerging. The structures correspond to shock fronts which gradually subsequently break up into smaller, possibly, eddy-like structures. This process becomes manifest in the flat-

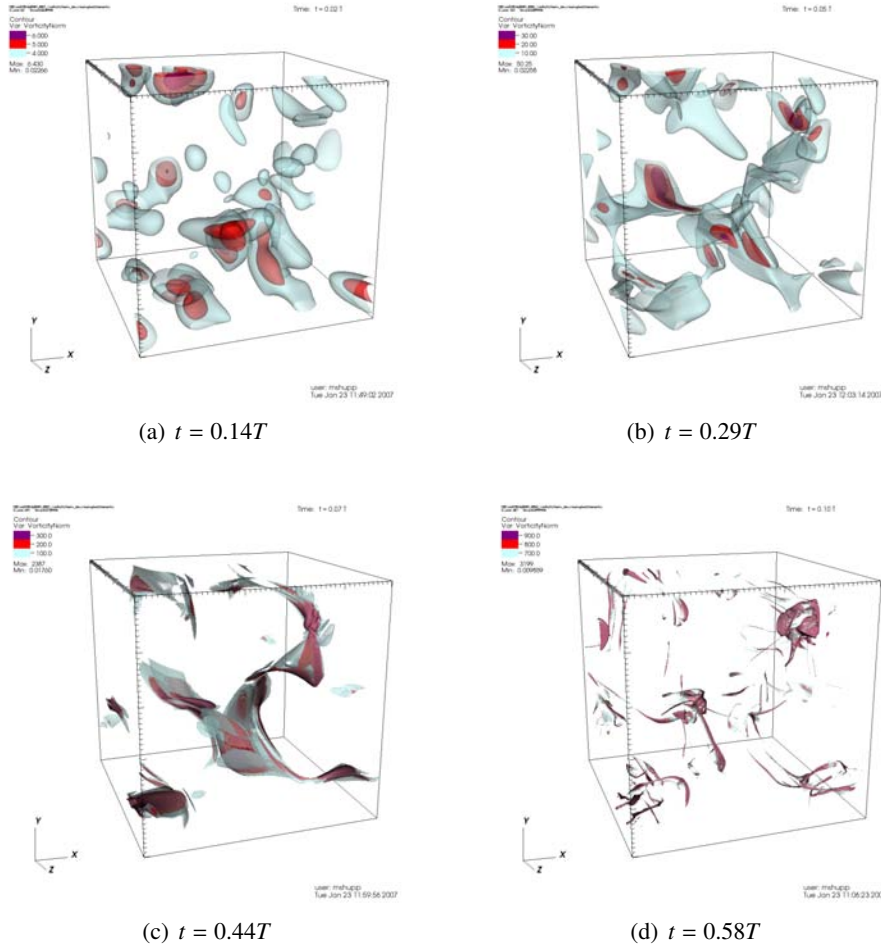


Figure 7: Isosurfaces of the vorticity modulus  $\omega$  at various instants of time.

tening of the energy spectrum functions.

### 3.2.4 Structure functions

The energy spectrum function  $E(k)$  specifies the scaling behaviour of the second moment of the velocity field in Fourier space. The corresponding description in physical space is the second order structure function, i. e., the spatial correlation function of the second moment of the velocity field. Structure functions of order  $p$  are generally defined by

$$S_p(l) \equiv \langle |\mathbf{v}(\mathbf{x} + \mathbf{l}) - \mathbf{v}(\mathbf{x})|^p \rangle_{\mathbf{x}} \sim l^{\zeta(p)}. \quad (7)$$

The computation of higher order structure functions is a computationally demanding task due to the very large amount of sampling points necessary to gain con-

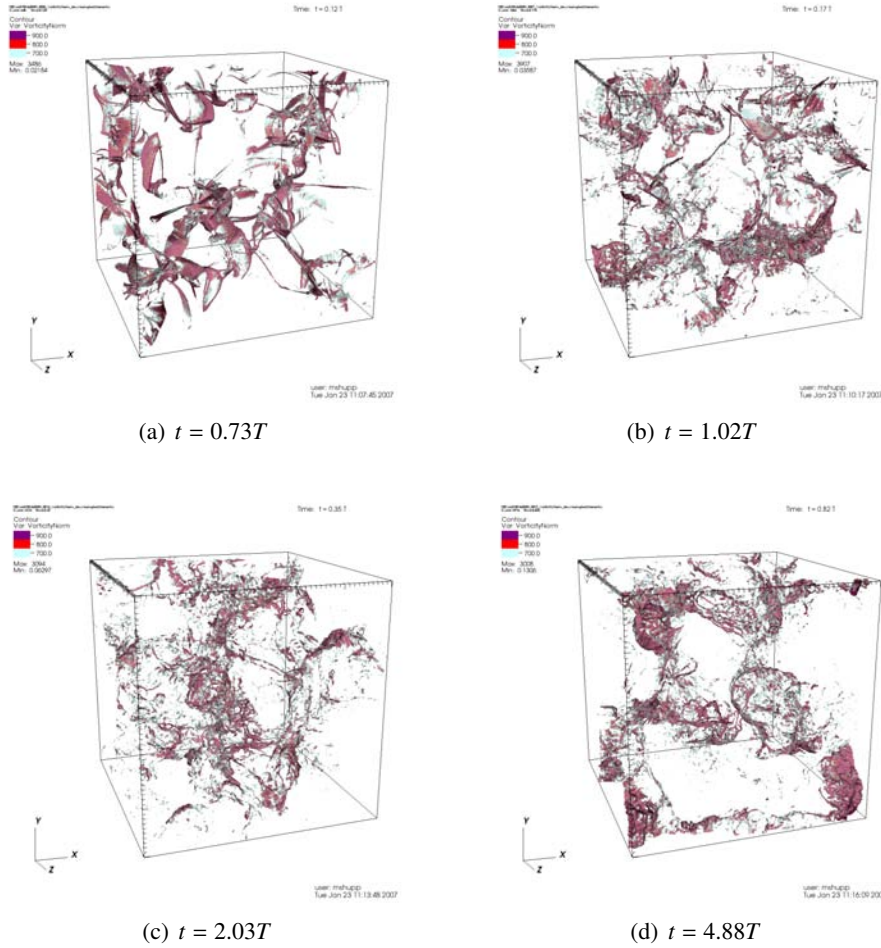


Figure 8: Figure 7 continued.

verged statistics. All results presented hereafter have been computed based on approximately  $2.4 \times 10^{10}$  data pairs. To ensure that sufficient numbers of data pairs were sampled, we increased the amount of sampled data by a factor of 5 in one particular case. No significant differences were found for the structure functions up to fifth order in this case.

We analysed the simulation data at six consecutive instants of time and fitted a power-law to the nearly inertial subrange  $8 \leq l \leq 70$ . Table 2 shows all scaling exponents  $\zeta(p)$  with  $p = 1, \dots, 5$ . Since the variations in time appear to be marginal, we averaged the values for each order  $p$ . Figure 9 shows our results for the transversal structure functions  $S_{p,\text{trans}}(l)$  up to order 5. The structure function scaling exponents obtained from fits and listed in Table 2 were averaged over time and normalised to the third order structure function exponent  $\zeta(3)$  for better com-

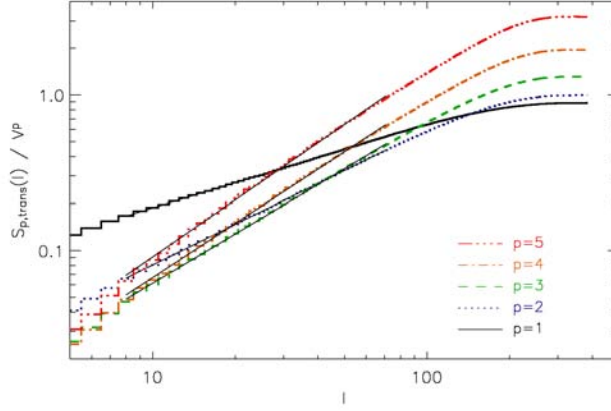


Figure 9: Transversal structure functions  $S_{p,\text{trans}}(l)$  normalised to the corresponding power of the velocity field. Thin black lines indicate the applied fits.

$t/T$	$p = 1$	$p = 2$	$p = 3$	$p = 4$	$p = 5$
2.03	$0.562 \pm 0.004$	$0.888 \pm 0.003$	$1.066 \pm 0.008$	$1.167 \pm 0.013$	$1.228 \pm 0.016$
3.05	$0.583 \pm 0.005$	$0.884 \pm 0.003$	$1.097 \pm 0.006$	$1.239 \pm 0.013$	$1.344 \pm 0.019$
4.06	$0.531 \pm 0.003$	$0.858 \pm 0.004$	$1.035 \pm 0.013$	$1.123 \pm 0.023$	$1.163 \pm 0.031$
4.93	$0.530 \pm 0.002$	$0.848 \pm 0.006$	$1.018 \pm 0.016$	$1.100 \pm 0.026$	$1.135 \pm 0.034$
5.95	$0.523 \pm 0.003$	$0.852 \pm 0.004$	$1.044 \pm 0.012$	$1.157 \pm 0.021$	$1.224 \pm 0.027$
6.96	$0.546 \pm 0.004$	$0.875 \pm 0.004$	$1.053 \pm 0.010$	$1.150 \pm 0.017$	$1.208 \pm 0.021$

Table 2: Fitted scaling exponents  $\zeta(p)$ ,  $p = 1, \dots, 5$ , for several stages of fully developed turbulence in the range of length scales  $8 \leq l \leq 70$ .

parison to other authors. We stress that the utilisation of the extended self similarity hypotheses [Benzi et al., 1993] was not necessary, since our data show clear scaling behaviour due to the rather large numerical resolution.

For comparison with theory, we consider the prediction of Boldyrev [2002], which is a generalisation of the She and Leveque [1994] theory for the scaling exponents in supersonic turbulence:

$$\zeta(p) = \frac{p}{9} + C \left( 1 - \left[ 1 - \frac{2}{3C} \right]^{p/3} \right) \quad (8)$$

The parameter  $C = 3 - D$ , where  $D$  is the fractal dimension of the dominating dissipative structures in the flow, is called the co-dimension. A common idea is that in the case of subsonic turbulence, energy is dissipated in vortex filaments or tubes with  $D = 1$ , whereas mostly sheet-like shocks with  $D = 2$  dissipate energy in supersonic turbulent flow. Boldyrev et al. [2002] report MHD simulations which yield scaling exponents very close to the theoretical prediction for  $D = 2$ . The

$p$	SL94 ( $C = 2$ )	B02 ( $C = 1$ )	BNP02	B02g ( $C = 0.7$ )	this work	
1	0.33	0.36	0.42	0.42	0.56	$0.51 \pm 0.02$
2	0.67	0.70	0.74	0.74	0.83	$0.83 \pm 0.02$
3	1.00	1.00	1.00	1.00	1.00	1.00
4	1.33	1.28	1.21	1.20	1.13	$1.10 \pm 0.05$
5	1.67	1.54	1.40	1.38	1.25	$1.16 \pm 0.07$

Table 3: Comparison of the scaling exponents  $\zeta(p)/\zeta(3)$  for structure functions of order  $p = 1, \dots, 5$  as predicted by the Kolmogorov [1941] (K41) theory and the She and Leveque [1994] (SL94) theory as well as the theoretical and numerical results by Boldyrev [2002] (B02, B02g), Boldyrev et al. [2002] (BNP02) together with our results.

scaling exponents obtained from our simulation, on the other hand, differ markedly from the Boldyrev [2002] theory for  $C = 1$  as well as from the numerical results of Boldyrev et al. [2002]. For an overview, see Table 3.

As regards differences between the numerical simulations, we note that Boldyrev et al. [2002] perform MHD simulations even though the ratio of magnetic to kinetic energy density is small ( $e_{\text{mag}}/e_{\text{kin}} \approx 0.1$ , [Padoan et al., 2004]) and the authors report on comparable results with even weaker magnetic fields. Their Mach numbers are  $\approx 10$ , while we use  $\text{Ma} \approx 5$ .

A significant difference, however, concerns the employed forcing mechanism. Boldyrev et al. [2002] use purely solenoidal forcing modes and find that the emerging compressible modes of the velocity field contain a rather small amount of energy,  $E_{\parallel}/E_{\perp}(k) \approx 0.1 - 0.2$ , in the inertial subrange, whereas predominantly dilatational forcing is applied in our simulation. A parameter study of LES of turbulence varying the forcing fields indicates that the forcing might very well influence the structure of the produced velocity field at scales much smaller than the integral scale [Schmidt and Federrath, 2007], resulting in an inertial subrange greatly affected by compressive modes in the case of a dilatational driving force, in contrast to the findings of Boldyrev et al. [2002].

A fit of the scaling exponents calculated from our simulation assuming the functional form (8) is plotted in Figure 10. The fit yields the co-dimension  $C = 0.70 \pm 0.07$  corresponding to  $D = 2.30 \pm 0.07$ . Remarkably, this result equals, within the error margin, the fractal dimension of the density field measured for interstellar gas [Elmegreen and Elmegreen, 2001; Chappell and Scalo, 2001], which is probably correlated to the fractal dimension of dissipative structures [Boldyrev, 2002; Ostriker et al., 2001; Larson, 1992].

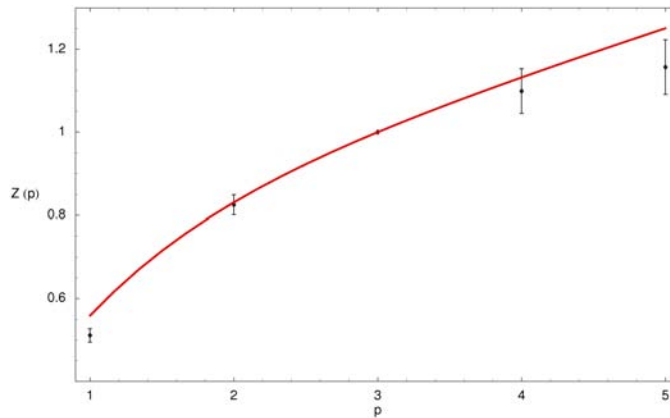


Figure 10: Fitting of the scaling exponents  $Z(p) = \zeta(p)/\zeta(3)$  from our data displayed in Table 3 by Equation (8) to determine the co-dimension  $C$ .

## 4 Simulations with adaptive mesh refinement

In the following, a case study of different refinement techniques in turbulence simulations featuring AMR with relatively low resolution is presented. Based on the outcome of this study, we performed high-resolution AMR simulations of adiabatic and isothermal turbulence, respectively.

### 4.1 Investigation of refinement criteria

We concentrated on refinement by the gradient of the velocity field, without explicitly resorting to the mass density. Rather than monitoring each component  $v_{i,j}$  of the velocity gradient, we formulated control variables in terms of scalars. Obvious candidates are the rate-of-strain scalar  $|S|$  and the vorticity modulus  $\omega$  (see Section 3.1.2 for definitions). The former includes the divergence of the velocity as trace contribution, i. e.,  $d = S_{ii}$ . The divergence accounts for compression effects, particularly, in the vicinity of shock fronts. Vortices, on the other hand, are identified by large values of  $\omega$ .

The simplest ansatz is to specify some global threshold value  $\Lambda$  such that grid cells will be flagged for refinement either if  $|S|^2 > \Lambda$  or if  $\omega^2 > \Lambda$ . For brevity, we denote this type of refinement by  $I_\Lambda$ . Using a root grid with  $N_0 = 96^3$  cells and one level of refinement at an effective resolution equivalent to  $N_{1,\text{eff}} = 192^3$ , three distinct values of the threshold  $\Lambda$  were tested for the adiabatic case. The outcome was compared to a reference simulation running on a static grid with  $N = 192^3$  cells. As diagnostic data, the probability density functions of  $\omega$  at subsequent instants of time are plotted in Figure 11. At early time, prior to the peak in the RMS Mach number, the pdfs are quite insensitive to the chosen thresholds. At later time, however, significant deviations from the reference pdfs become apparent

for  $\Lambda = 300$  and  $\Lambda = 1000$ , respectively, while excellent agreement of the high-vorticity tails is achieved with the criterion  $I_{100}$ . Evidently, the growth of small-scale structure will be suppressed if the threshold for refinement is chosen too high, because thin vortex filaments are not captured by refined grid patches. However, the case  $I_{100}$  does not avail either, because of an overproduction of refined grid patches. This is illustrated by the volume filling factors of the refined grid patches listed in Table 4. As one can see, a very delicate balancing of the threshold value would be required.

Table 4: Volume filling factors of grid patches at the first level of refinement for the same AMR runs as in Figure 11

refinement criterion	$\chi_1(0.48)$	$\chi_1(1.02)$	$\chi_1(3.01)$
$I_{100}$	0.555	0.960	0.991
$I_{300}$	0.293	0.512	0.274
$I_{1000}$	0.002	0.000	0.001

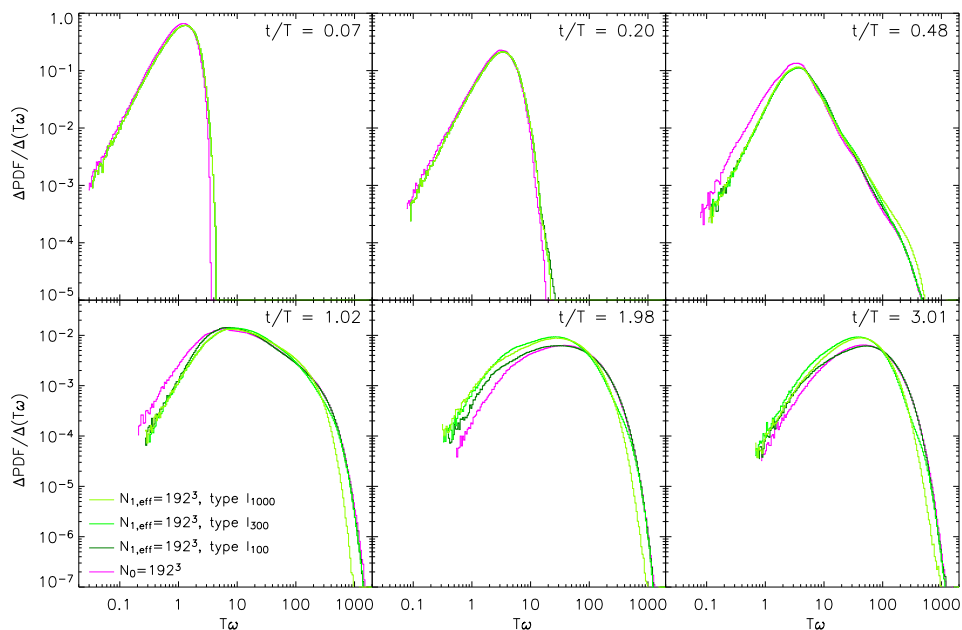


Figure 11: Probability density functions of the vorticity modulus  $\omega$  in adiabatic turbulence simulations. Shown are the results from three AMR test runs with refinement by global thresholds of  $|S|$  and  $\omega$  and, as reference, the pdfs calculated from a static grid simulation.

Table 5: Volume filling factors of the refined grid level in the AMR runs of Figure 11

refinement criterion	$\chi_1(0.48)$	$\chi_1(1.02)$	$\chi_1(3.01)$
$\Pi_{0.5\lambda}$	0.414	0.818	0.957
$\Pi_{1.0\lambda}$	0.354	0.717	0.854
$\Pi_{2.0\lambda}$	0.280	0.518	0.595
$\Pi_{3.0\lambda}$	0.230	0.365	0.378
$\Pi_{10.0\lambda}$	0.060	0.024	0.031

In the case of a positive control variable such as the vorticity, the typical magnitude is specified by the spatial mean. Thus, a global threshold for refinement has to be chosen close the mean. Otherwise, most regions would be missed out if the threshold was significantly greater than the mean or, if the threshold was too low, over-refinement would result. Consequently, some normalisation might be introduced. An option that suggests itself is to normalise derived quantities such as the vorticity by the local value of the primitive and the cutoff length. So refinement would be triggered if  $\omega$  became greater than a certain multiple of  $v/\Delta_n$ , where  $\Delta_n$  is the cell size at the  $n$ -th level of refinement. Let us consider what this kind of refinement implies in the case of subsonic isotropic turbulence obeying Kolmogorov-Obukhov scaling. Then the RMS velocity fluctuations at length scale  $\ell$  fulfil the power law  $v'(\ell) \sim \ell^{1/3}$ . For a grid patch of resolution  $\Delta_n$ , it follows that velocity increments between neighbouring grid cells  $\delta v \sim V(\Delta_n/L)^{1/3}$ , where  $V$  is the characteristic velocity and  $L$  is the integral length. Refinement would be triggered whenever the normalised gradient  $\delta v/v$  was greater than a prescribed constant. Since  $v \sim V$ , we have  $\delta v/v \sim (\Delta_n/L)^{1/3}$ , implying that the likelihood of refinement differs for grids of varying resolution. This is an undesired property.

An alternative approach is the comparison of a control variable with statistical moments, particularly, the mean and the standard deviation. For a positive quantity like the vorticity, the mean is an appropriate measure of the typical magnitude. In the case of a quantity exhibiting large fluctuations between negative and positive values, however, one might rather consider the standard deviation. We propose to generically compare a control variable modulo its mean to multiples of the mean and the standard deviation, where the maximum of both is decisive. Thus, the threshold for a generic control variable  $f(\mathbf{x}, t)$  is given by a multiple of

$$\lambda_i(t) := \max[\langle f \rangle_i(t), (\sigma_i^{1/2} f)(t)], \quad (9)$$

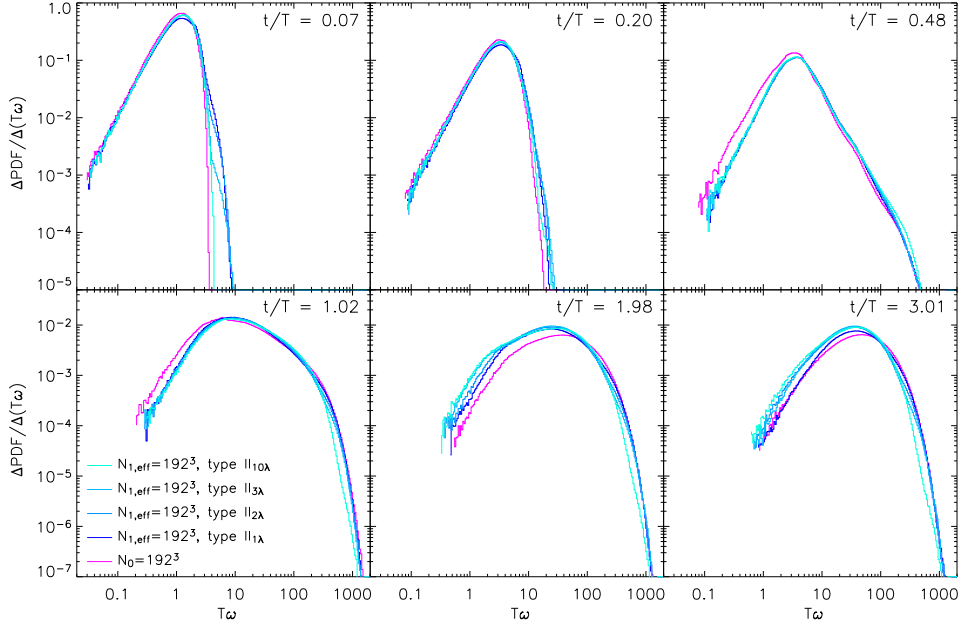


Figure 12: Probability density functions of the vorticity modulus  $\omega$  in adiabatic turbulence simulations. Shown are several AMR test runs with refinement by the local variability of  $|S|$  and  $\omega$  together with the simulation using a static grid.

where  $\langle f \rangle_i(t)$  denotes the spatial mean of  $f(\mathbf{x}, t)$  on the  $i$ -th grid patch and  $(\sigma_i f)(t) = \langle f^2 \rangle_i(t) - \langle f \rangle_i^2(t)$  is the variance. The calculation of the statistical moments is constrained to single grid patches, because the flow, in general, can be inhomogenous. Thus, a cell will be flagged for refinement if

$$f(\mathbf{x}, t)|_{\mathbf{x} \in G_i} \geq \langle f \rangle_i(t) + C\lambda_i(t). \quad (10)$$

As shortcut for refinement by the *regional variability* of the control variable, we write  $\Pi_{C\lambda}$ .

In a series of test simulations, we investigated refinement by the regional variability of  $|S|^2$  and  $\omega^2$ . The resulting  $\omega$ -pdfs are plotted in figure 12 and a selection of volume filling factors is listed in table 5. Good agreement in comparison to the static grid run is achieved with  $C \sim 1$ . As opposed to type I refinement, *a priori* knowledge about the rate of strain and the vorticity is not required. In figures 15 and 16, one can see visualisations of vorticity isosurfaces and volume renderings of the divergence. Both figures compare the static grid simulation with the AMR run using the refinement criterion  $\Pi_{1.0\lambda}$ . The plots on top of each figure correspond to the maximal RMS Mach number at  $t \approx 0.5T$ . Although some spurious vorticity can be discerned in the AMR run, the agreement is excellent. Spurious vorticity is inherent to fluid dynamical simulations with AMR, as reported by Plewa and Müller [2001], because the boundaries between grid patches of different resolution

inevitably introduce discontinuities. Naturally, this effect is more noticeable in flow derivatives rather than in primitives. At later stages, the spurious vorticity becomes negligible. Due to the non-linearity of developed turbulence, however, exact agreement of the flow realization diminishes. Nevertheless, the pdfs demonstrate that the statistical properties of the flow realizations are basically the same.

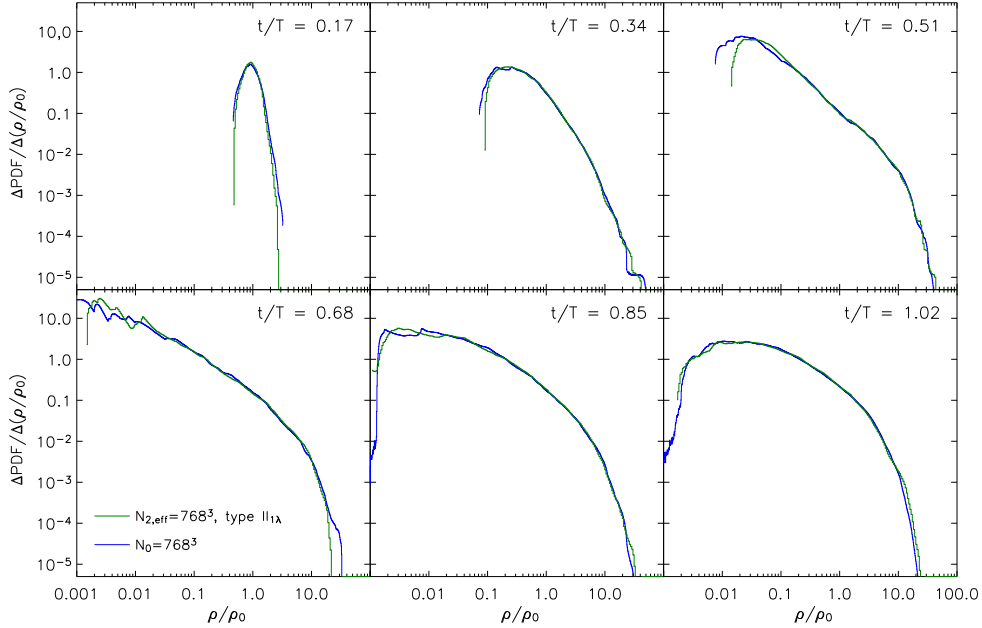


Figure 13: Probability density functions of the mass density in simulations of forced isotropic turbulence.

## 4.2 Production runs

We performed two big AMR simulations with refinement by regional variability and effective resolution equal to the static grid simulations discussed in Section 3. In both simulations, root grids of  $N_0 = 192^3$  cells were used. For adiabatic turbulence, there were two refined grid levels with  $N_{1,\text{eff}} = 384^3$  and  $N_{2,\text{eff}} = 768^3$ , respectively, whereas we opted for only one refined level with  $N_{1,\text{eff}} = 768^3$  corresponding to  $\Delta_1/\Delta_0 = 1/4$  in the case of isothermal turbulence. Unfortunately, the latter choice posed severe difficulties in adapting the postprocessing tools. Since a satisfactory solution was not achieved at the time of the writing of this report, we restrict the discussion to the adiabatic turbulence simulation. Even in this case, there were some problems with the postprocessing. In particular, for two levels of refinement, we were not able to compute the vorticity correctly because of shortcomings in the algorithm that projects the various fields from the adaptive grid

hierarchy onto uniform grids. This is why the pdfs of the mass density at several stages within the first integral time are plotted in Figure 13. As one can see, the agreement with the pdfs predicted by the static grid simulation is excellent.

Unfortunately, the present version of Enzo is not very efficient in working with an extremely large number of grid patches. In part, this is caused by the grid generation algorithm, which is likely to improve in upcoming versions of the code. As a workaround for the time being, the threshold factor  $C$  of the  $\Pi_{C\lambda}$  criterion was increased in several steps from the initial value 1.0 to 3.0 from  $t = 0.66T$  onwards. Even with the relatively high threshold factor  $C = 3.0$ , the total number of grid patches amounted to 18111 at time  $t = 1.02T$ . Volume filling factors of 40% at the first level and 19.2% at the second level of refinement were found for this particular grid hierarchy.

Telling from the case study in Section 4.1, one would expect to miss out a significant fraction of small scale structure for  $C = 3.0$ . Since the vorticity pdfs are not available yet, we consider structure functions here. Figure 14 shows several plots, in which the structure functions of order 1, 2 and 5 are compared at  $t = 0.5T$  and  $t = 1.0T$ , respectively. The first instant of time corresponds to the peak in the mean Mach number, where the flow is dominated by shock fronts at large scales, while smaller vortices are forming and the flow is evolving towards the transonic regime at time  $t = 1.0T$  (see Figures 1 and 16 a & b). For  $t = 0.5$ , one can see an almost perfect match of the structure functions obtained from the static grid simulation and the AMR simulation, respectively. One should note that  $C = 1.0$  in this case. For  $t = 1.0$ , the structure functions resulting from the AMR simulation fall off slightly steeper towards decreasing length scales. It appears that setting  $C = 3.0$  causes a moderate loss of small scale velocity fluctuations which affects the structure functions, whereas virtually no influence on the distribution of mass density can be discerned.

## 5 Conclusion

In our DECI project, we investigated new techniques for the numerical simulation of turbulence. The basic idea, namely, applying adaptive mesh refinement to turbulent flow, has been exploited before [Kritsuk et al., 2006]. We attempted to develop this approach further. Ultimately, the methodology is intended for various astrophysical applications.

We were able to finish the first phase formulated in our description of enabling work within the duration of the DECI project. This phase included four major numerical simulations of forced supersonic turbulence which exhausted the budget of 300.000 CPU-hrs allocated to the project. An advanced forcing scheme was utilised that differs from the conventional, purely solenoidal forcing. In two simulations, the adiabatic and the isothermal case were investigated using static grids. These simulations yielded reference data for comparisons with the following adaptive mesh refinement (AMR) simulations.

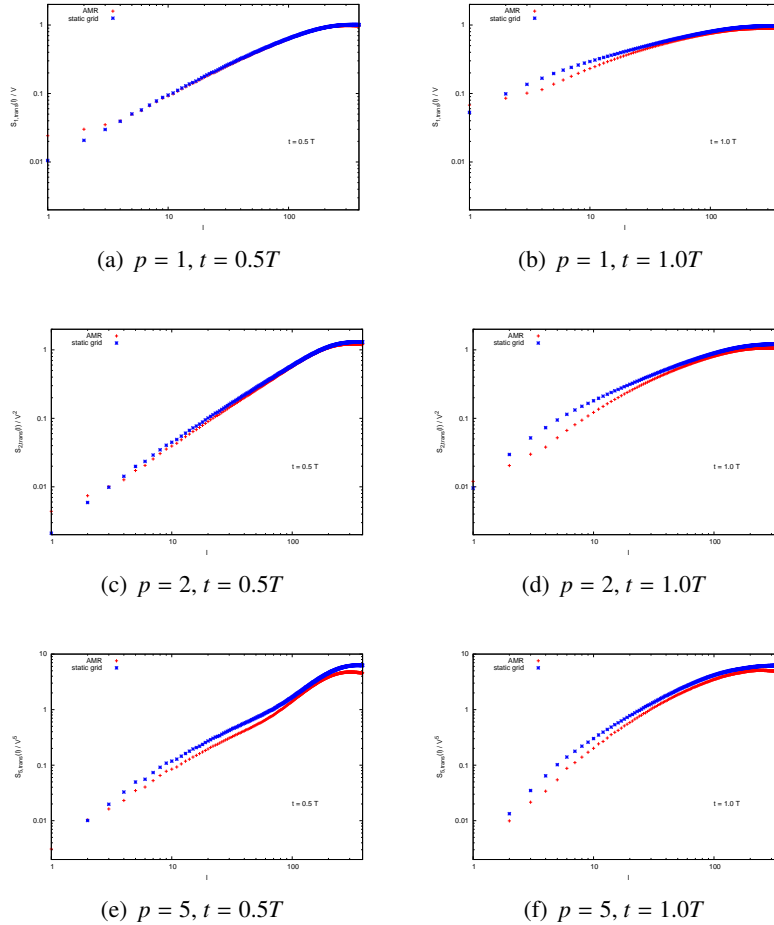


Figure 14: Structure functions in high-resolution simulations of adiabatic turbulence.

The data produced in these simulations are worthwhile for scientific exploitation in its own right. We demonstrated that care must be taken in applying fit functions such as the lognormal fit to probability density functions of mass density. Especially in the high-density tails that are relevant to star formation, significant deviations are possible. Moreover, the scaling exponents of structure functions found in our simulation do not agree with theoretical predictions that are commonly adopted in astrophysical applications. It appears that the values of the scaling exponents are not universal with respect to the properties of the forcing field. This result is particularly interesting since turbulence in the interstellar mediums is not likely to be generated by purely solenoidal forcing. Contrasting adiabatic and isothermal turbulence, it can be seen that the thermodynamical properties of the gas are crucial for the behaviour of supersonic turbulent flow.

Performing numerous test simulations, each one consuming a few thousand CPU-hrs only, we systematically explored various techniques of triggering the generation of refined grid patches. Other than Kritsuk et al. [2006], we formulated refinement criteria that are not only sensitive to the formation of shocks in supersonic flow but also track vortices. The versatility of these criteria was demonstrated in a highly resolved simulation of adiabatic turbulence, in which a transition from supersonic to mostly subsonic flow occurred. In particular, we found that probability density functions of mass density and structure functions were well reproduced in comparison to the static grid simulation.

In the accompanying isothermal turbulence simulation, a different refinement criterion based on the rate of compression was applied. Because of the factor 4 between the resolutions of adjacent grid levels in this simulation, we still have to work out major modifications of our postprocessing tools. The larger scaling factor (a factor of 2 was used in the adiabatic turbulence simulation) allowed for a greatly enhanced performance. The results will be presented in a planned publication.

Since it is generally impossible to treat turbulence at all length scales by means of AMR only, the next step will be to combine AMR with the subgrid scale model formulated by Schmidt et al. [2006]. This will link conventional AMR to LES and, therefore, we call the new method Fluid mEchanics with Adaptively Refined Large Eddy SimulationS (FEARLESS). The numerical study carried out in the framework of DECI laid the foundation. In follow-up projects, the turbulent interstellar medium, the evolution of spiral galaxies with feedback from star formation and the dynamics of hot gas in galaxy clusters will be investigated with FEARLESS. Preliminary tests of the new refinement criteria, for instance, in galaxy cluster simulations, showed that good performance can be achieved while substantially richer turbulent flow structure emerges. In conclusion, we expect that FEARLESS will open new perspectives in astrophysics by the as yet unequalled level of sophistication in the treatment of turbulence.

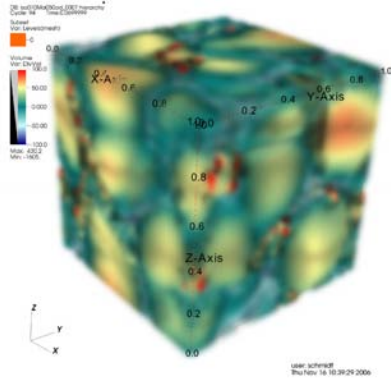
## References

- Benzi, R., S. Ciliberto, R. Tripicciono, C. Baudet, F. Massaioli, and S. Succi (1993). Extended self-similarity in turbulent flows. *Phys. Rev. E* 48, 29.
- Berger, M. J. and P. Colella (1989). Local Adaptive Mesh Refinement for Shock Hydrodynamics. *J. Comp. Physics* 82, 64–84.
- Berger, M. J. and J. Oliger (1984). Adaptive Mesh Refinement for Hyperbolic Partial Differential Equations. *J. Comp. Physics* 53, 484–512.
- Boldyrev, S. (2002). Kolmogorov-Burgers Model for Star-forming Turbulence. *Astrophys. J.* 569, 841–845.
- Boldyrev, S., A. Nordlund, and P. Padoan (2002). Scaling Relations of Supersonic Turbulence in Star-forming Molecular Clouds. *Astrophys. J.* 573, 678–684.

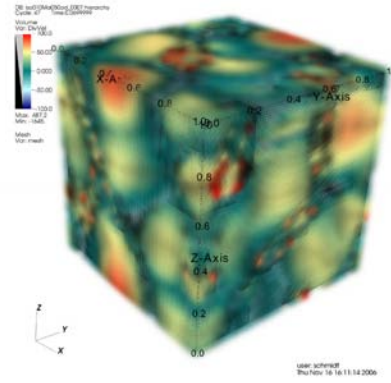
- Chappell, D. and J. Scalo (2001). Multifractal Scaling, Geometrical Diversity, and Hierarchical Structure in the Cool Interstellar Medium. *Astrophys. J.* 551, 712–729.
- Colella, P. and P. R. Woodward (1984). The piecewise parabolic method (PPM) for gas-dynamical simulations. *J. Comp. Physics* 54, 174–201.
- Elmegreen, B. G. and D. M. Elmegreen (2001). Fractal Structure in Galactic Star Fields. *Astron. J.* 121, 1507–1511.
- Kolmogorov, A. N. (1941). . *Dokl. Akad. Nauk SSSR.* 32, 16.
- Kritsuk, A. G., M. L. Norman, and P. Padoan (2006, February). Adaptive Mesh Refinement for Supersonic Molecular Cloud Turbulence. *Astrophys. J. Lett.* 638, L25–L28.
- Larson, R. B. (1992). Towards understanding the stellar initial mass function. *MNRAS* 256, 641–646.
- Norman, M. L. (2004). The Impact of AMR in Numerical Astrophysics and Cosmology. Preprint astro-ph/0402230.
- O’Shea, B. W., G. Bryan, J. Bordner, M. L. Norman, T. Abel, R. Harkness, and A. Kritsuk (2004). Introducing Enzo, an AMR Cosmology Application. To appear in “Adaptive Mesh Refinement - Theory and Applications”, Eds. T. Plewa, T. Linde & V. G. Weirs, Springer Lecture Notes in Computational Science and Engineering, 2004.
- Ostriker, E. C., J. M. Stone, and C. F. Gammie (2001). Density, Velocity, and Magnetic Field Structure in Turbulent Molecular Cloud Models. *Astrophys. J.* 546, 980–1005.
- Padoan, P., R. Jimenez, A. Nordlund, and S. Boldyrev (2004). Structure Function Scaling in Compressible Super-Alfvénic MHD Turbulence. *Phys. Rev. Lett.* 92(19), 191102–+.
- Padoan, P. and A. Nordlund (2002). The Stellar Initial Mass Function from Turbulent Fragmentation. *Astrophys. J.* 576, 870–879.
- Plewa, T. and E. Müller (2001, August). AMRA: An Adaptive Mesh Refinement hydrodynamic code for astrophysics. *Computer Physics Communications* 138, 101–127.
- Schmidt, W. and C. Federrath (2007). A parameter study of forced supersonic turbulence in large eddy simulations. in preparation.
- Schmidt, W., W. Hillebrandt, and J. C. Niemeyer (2006). Numerical dissipation and the bottleneck effect in simulations of compressible isotropic turbulence. *Comp. Fluids.* 35, 353–371.

Schmidt, W., J. C. Niemeyer, and Hillebrandt (2006). A localised subgrid scale model for fluid dynamical simulations in astrophysics. I. Theory and numerical tests. *Astron. & Astrophys.* 450, 265–281 & 283–294.

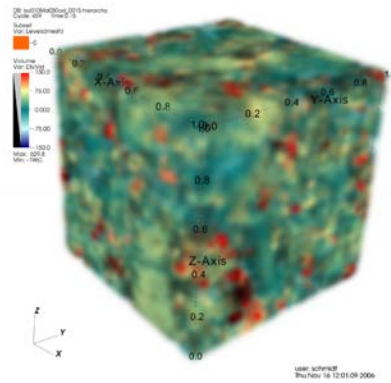
She, Z.-S. and E. Leveque (1994). Universal scaling laws in fully developed turbulence. *Phys. Rev. E.* 72, 336–339.



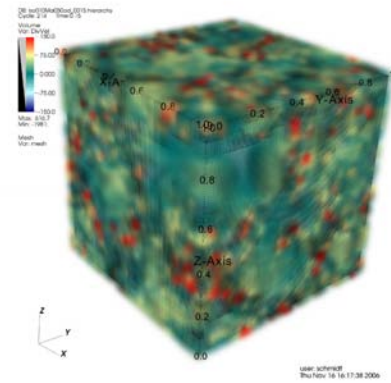
(a) static run,  $t = 0.5T$



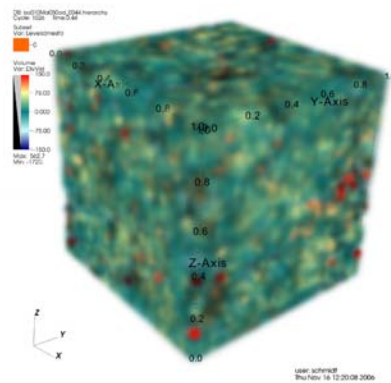
(b) AMR run,  $t = 0.5T$



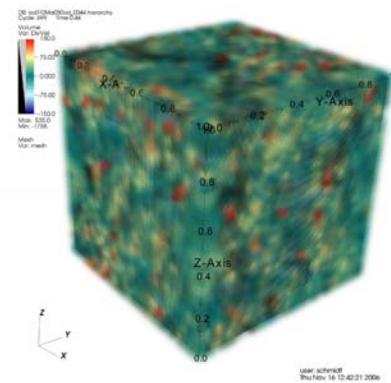
(c) static run,  $t = 1.0T$



(d) AMR run,  $t = 1.0T$

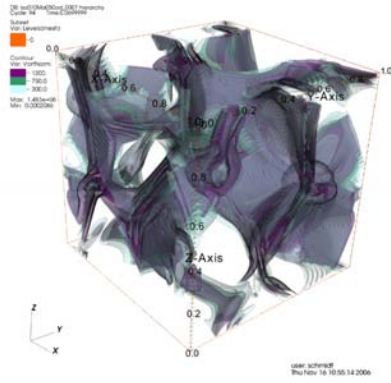


(e) static run,  $t = 3.0T$

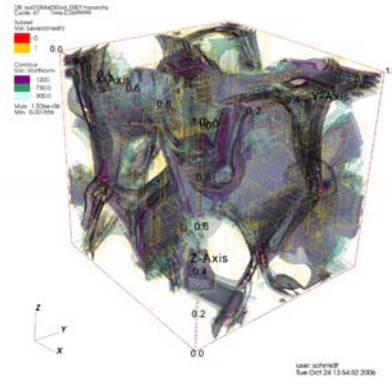


(f) AMR run,  $t = 3.0T$

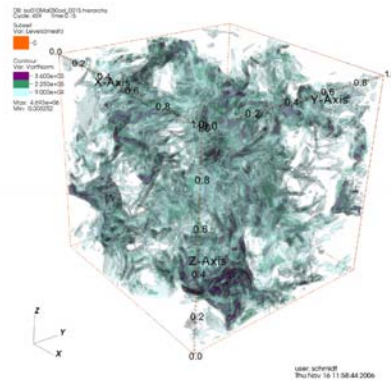
Figure 15: Comparison of divergence volume renderings for a static grid (left column) and an AMR (right column) simulation of equal effective resolution.



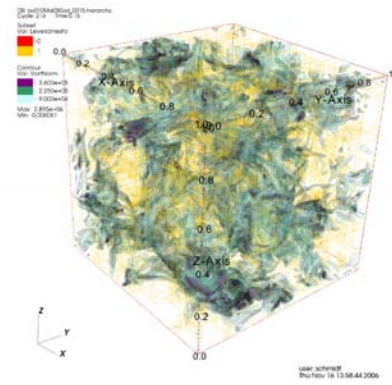
(a) static run,  $t = 0.5T$



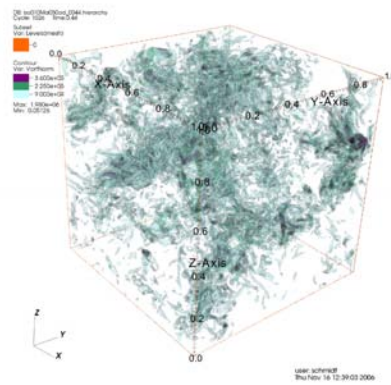
(b) AMR run,  $t = 0.5T$



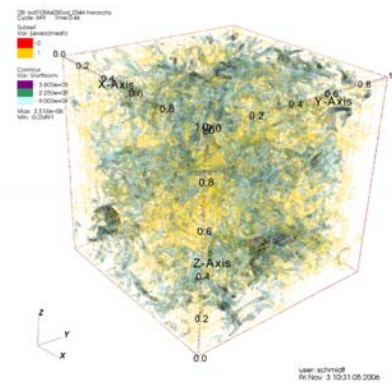
(c) static run,  $t = 1.0T$



(d) AMR run,  $t = 1.0T$



(e) static run,  $t = 3.0T$



(f) AMR run,  $t = 3.0T$

Figure 16: Comparison of vorticity isosurfaces for a static grid (left column) and an AMR (right column) simulation of equal effective resolution.